Simulations of microlayer formation in nucleate boiling

Alexandre Guion [a,*], Shahriar Afkhami [b], Stéphane Zaleski [c], Jacopo Buongiorno [a]

[a] Department of Nuclear Science and Engineering, Massachusetts Institute of Technology, Cambridge, MA, USA
[b] Department of Mathematical Sciences, New Jersey Institute of Technology, Newark, NJ, USA
[c] Sorbonne Université, CNRS, Institut Jean le Rond d'Alembert, UMR 7190, F-75005, Paris, France

ABSTRACT

As a bubble grows outside of a cavity during nucleate boiling, viscous effects can be large enough compared to surface tension to impede liquid motion and trap a thin liquid layer, referred to as the microlayer, underneath the growing bubble. Numerical simulations of nucleate boiling typically resolve the macroscopic liquid-vapor interface of the bubble, but resort to subgrid models to account for micro scale effects, such as the evaporation of the microlayer. Evaporation models require initialization of the microlayer shape and extension, but models for microlayer formation are either physically incomplete or purely empirical. In this work, the Volume-Of-Fluid (VOF) method, implemented in the Gerris code, is used to numerically reproduce the hydrodynamics of hemispherical bubble growth at the wall, and resolve the formation of the microlayer with an unprecedented resolution. The simulations are validated against the latest experimental data and compared to existing analytical models. Lastly, remaining gaps in building a generally applicable model for the formation of the microlayer are presented.

© 2018 Published by Elsevier Ltd.

1. Introduction and motivation

The transport of latent heat makes boiling one of the most efficient mode of heat transfer, allowing a wide range of systems to improve their thermal performance, from nuclear power plants to microelectronic devices - see reviews by [1–3]. Subcooled boiling heat transfer for example is able to accommodate very high heat fluxes, thus cooling components very efficiently.

Predicting boiling heat transfer has therefore garnered significant attention, but remains complicated by the need to consider phenomena occurring over multiple scales (see Fig. 1), from the adsorbed liquid layer at the wall at the nanometer scale - see [4,5], up to the bubble diameter at the millimeter scale, see [6–18].

1.1. Physical phenomena

During nucleate boiling a bubble grows outside of a surface imperfection, referred to as cavity, and from a preexisting embryo of vapor initially trapped in that surface imperfection. Boiling starts at the wall when the local temperature is sufficiently high to allow the vapor bubble to exist and grow outside of the cavity and into the surrounding liquid, see [19].

At the inception of nucleate boiling at a cavity, the liquid in the vicinity of the heated wall is superheated and mass transfer occurs at the liquid-vapor interface of the bubble. The growth of the bubble is also fueled by the overpressure within the vapor, and impeded by the inertia of the liquid. During this initial phase of rapid growth, often referred to as the inertia-controlled phase of bubble growth, the bubble grows hemispherically, i.e. bubble growth rates, U_b, based on bubble cross section area, bubble height, and bubble width are identical as shown in Fig. 2.

We define a capillary number Ca associated with the bubble growth rate as:

$$Ca = \mu_l U_b / \sigma$$

with μ_l the liquid viscosity and σ the surface tension coefficient. As the bubble grows outside of the cavity, Ca can be large enough to impede liquid motion at the wall and trap a thin liquid layer underneath the bubble, known as the liquid microlayer - see experimental evidence by [12,15,20–35]. After its formation, the microlayer begins to evaporate, which contributes to the bubble growth.

Once the bubble has reached a certain size, referred to as departure diameter, the bubble departs from its initial position at the heated wall and additional cooling mechanisms such as transient conduction and free convection can occur.

Based on the measurements of microlayer thickness versus time by [30] in the case of water at atmospheric pressure, we identify

---

* Corresponding author.
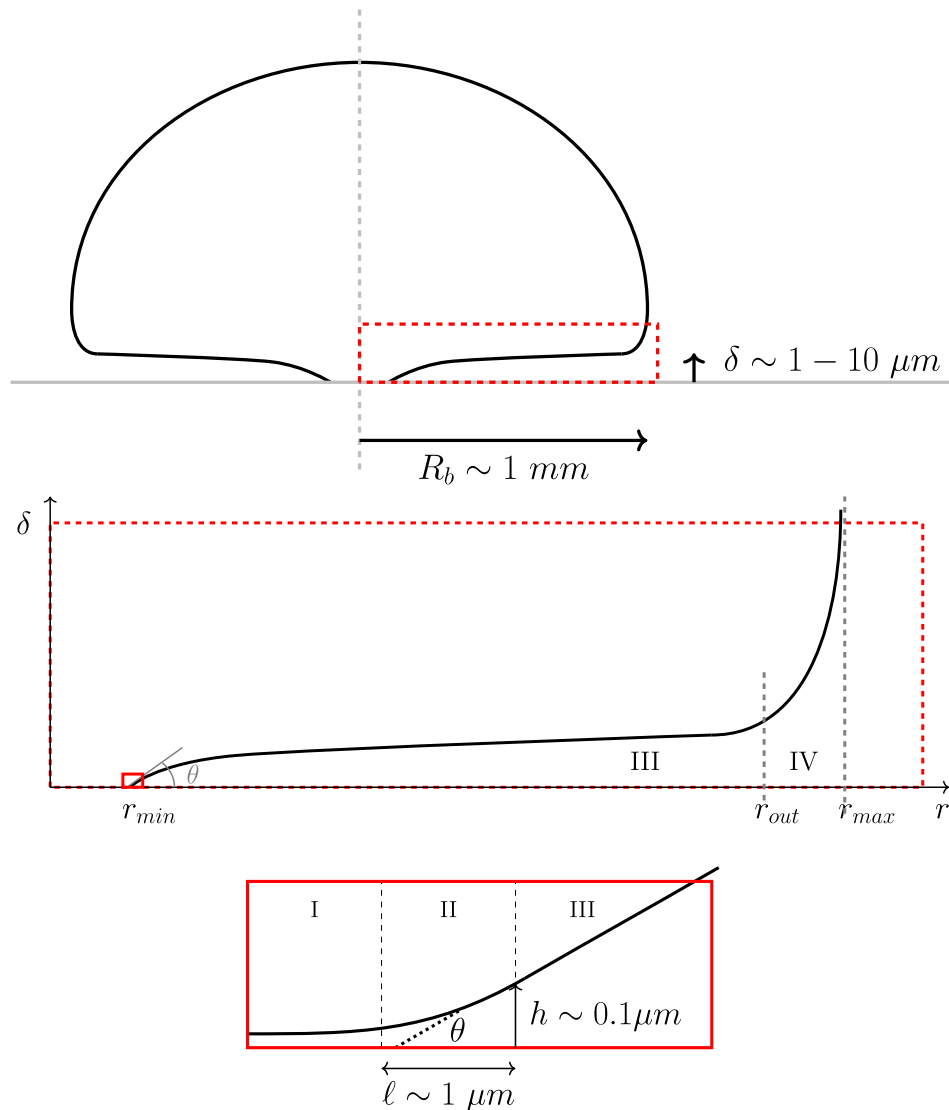 *E-mail address:* aguion@mit.edu (A. Guion).

Fig. 1. Multiple scales involved in nucleate boiling: from the millimeter scale at the bubble cap to the nanometer scale at the adsorbed liquid layer. Region I: adsorbed layer region of thickness $h_0 \sim 1-10$ nm. Region II: transition region between the non-evaporating adsorbed layer and the evaporating liquid microlayer ($h_0 < h < 100$ nm). Region III: central microlayer region of typical thickness $\delta \sim 1 - 10 \mu m$. Note in the bottom insert the black dotted line that represents the Triple Phase Line (TPL) where the three phases (liquid, vapor, and solid) are in apparent contact. The contact angle θ represents the angle between the contact line and the substrate at the microscopic scale. Region IV: microlayer outer-edge region of typical thickness $\delta \geqslant 10$ μm, where the thickness rapidly increases from the central region to the bubble cap.

two separate time scales τ_1 and τ_2 representative of microlayer formation and evaporation, respectively: $\tau_1 \sim 10-100$ μs, and $\tau_2 \sim 1-10$ ms.

1.2. Modeling of boiling heat transfer

For decades various empirical correlations and mechanistic models have been proposed to describe and predict boiling heat transfer for a wide range of boiling surface geometries, materials, working fluids, and operating conditions - see reviews by [2,6,36]. Of particular interest are the heat partitioning models described in [26,37,38] which aim to provide a mechanistic description of the wall boiling phenomena: the total heat flux at the wall is divided into separate heat flux components that account for various modes of heat transfer at the wall, such as forced convection, evaporation, quenching, and sliding conduction. In this context, recent advanced diagnostics (Infrared Imagery, Particle Image Velocimetry, High Speed Video Imagery, etc.) provide new and highly-resolved experimental data that can inform and validate models or correlations describing each individual component of the wall heat flux, as they individually represent a single specific physical phenomenon at the wall - see the review by [39]. Through careful calibration and post-processing, it is possible to accurately measure the temperature and heat flux distributions on the boiling surface which reveals detailed features, including the effects of evaporation of the liquid microlayer as shown by [8,40]. Depending on the fluid, flow and nucleation temperature, the contribution from microlayer evaporation to overall heat transfer and bubble growth can be large, e.g. in the case of water, see [40], or relatively small, e.g. in the case of refrigerants, see [8]. Typical microlayer models focus on evaporation at the Triple-Phase-Line (TPL) region where the three phases (liquid, solid, and vapor) are in apparent contact, see [9,41], or in the extended microlayer region, see [10,11,13]. In practice, numerical simulations of boiling resolve the macroscopic liquid vapor interface of boiling bubbles, but typically resort to subgrid models to include contributions at the microscopic scale such as from evaporation of the microlayer, which requires initialization of the microlayer shape and extension.
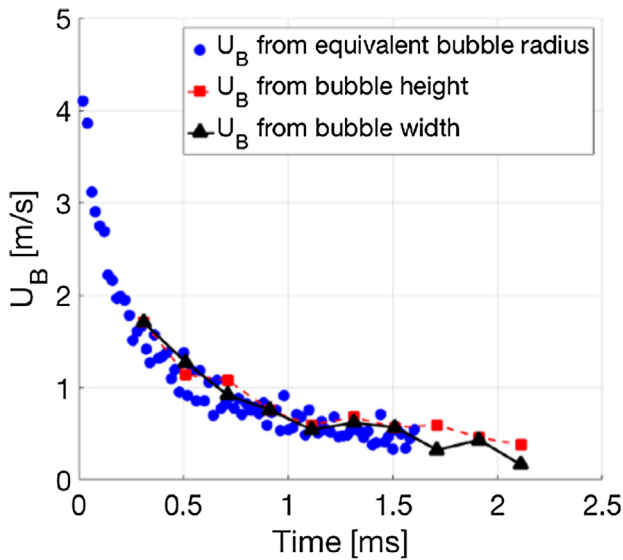
Fig. 2. Bubble growth rate U_b as a function of time based on bubble cross section area, bubble height, and bubble width recorded by a High Speed Video camera on the side of the growing bubble (Courtesy of Prof. Hyungdae Kim). Fluid is water at saturation and atmospheric pressure. Typical time scales $\tau_1 \sim 10-100\,\mu s$, and $\tau_2 \sim 1-10\,ms$ are representative of microlayer formation and evaporation, respectively.

1.3. Current gaps and proposed strategy

Existing models of microlayer formation are either physically incomplete, e.g. do not include the effect of surface tension or contact angle, see [42], or are purely empirical, see [13]. Existing experimental data that directly measures microlayer thickness profiles, see work from [12,25,27,30,32], does not cover a wide range of fluids and surfaces, which makes it difficult to generate or validate a general model on microlayer formation. In practice, measurements of microlayer thickness profiles are mostly obtained at times where the microlayer has already started to evaporate, with little insight on its formation dynamics. Recent advances by [35] in indirect measurements of microlayer thickness at short time scales can offer new insights and will be discussed.

In the present work, we use Computational Fluid Dynamics with Interface Tracking Methods to numerically reproduce the hydrodynamics of bubble growth at a wall, and resolve the formation of the liquid microlayer at the wall for a wide range of conditions and fluids. For all simulated cases, the Volume-Of-Fluid Method implemented in the Gerris flow solver from [43] is used to accurately track the liquid vapor interface over time, and predict the formation of the microlayer. We build a large numerical database from which microlayer formation models can be extracted.

1.4. Assumptions made in this work

In this work, we focus on the mechanisms of microlayer formation. In particular, we only consider the hydrodynamics of bubble growth at the wall, and neglect thermal effects, separating microlayer formation ($\tau_1 \sim 10-100\,\mu s$) from microlayer evaporation ($\tau_2 \sim 1-10\,ms \gg \tau_1$). Part of the liquid layer that forms at the wall may also evaporate during such short time scales τ_1, hence affecting its shape over time. However, we estimate that only 10% or less of the thickness of the liquid microlayer would be affected by evaporation during the formation phase, for a typical superheat at the wall ΔT_{sat} ($\Delta T_{sat} = 1$ to 10 K) observed experimentally at atmo-

spheric pressure, and considering evaporation from pure conduction through the liquid layer, for various growth times (1 to 100 μs), and various layer thicknesses (0.1 to 10 μm). Thermal effects, including the effect of mass transfer, on the motion of the contact line at short time scales are not included in the scope of the present work. Long range interaction forces of the liquid film with the substrate are also neglected as they may be relevant only at very short time scales where the film is very thin - see for example [44]. In this work, we implement a static contact angle at the wall for simplicity, which allows the contact line to move. However, one could replace it with a specific mobility law that would describe the behavior of the microscopic contact angle in the conditions of interest. Mesh dependence of moving contact lines simulations with grid size as previously shown by [45–47] is reported elsewhere, see [48].

1.5. Contributions and structure of the paper

This work focuses on three main objectives: (i) identify the minimum set of dimensionless parameters governing the hydrodynamics of microlayer formation at the wall during nucleate pool boiling, (ii) generate a numerical database that resolves the dynamics of microlayer formation for a broad range of conditions of interest (e.g. from water in lab experiment at atmospheric pressure, to water at nuclear reactor pressure conditions), and (iii) identify the remaining gaps in building a generally applicable model for microlayer formation, to be used during the initialization of boiling simulations. This paper specifically focuses on the central microlayer region, see region III in Fig. 1. Future work includes modeling the outer-edge region, see region IV in Fig. 1, using the present numerical database, and modeling the particular contact line dynamics using experimental data for specific wall conditions and for the fluid/solid pair of interest.

In Section 2 we provide a dimensional analysis and general functional dependence for the microlayer formation dynamics. In Section 3 we describe the computational framework used to simulate microlayer formation, and verify the correct implementation and convergence of the methods used. In Section 4 we discuss the reduction of the parameter space, qualitative trends and numerical results, and we compare our results in the central region (region III, Fig. 1) with the analytical model from [49] and with latest experimental results measuring microlayer thickness at early times. In Section 5 we conclude by discussing the contributions of this present work and the remaining opportunities for future work.

2. Problem statement and dimensional analysis

We consider the early growth of a steam bubble near the wall of a pool of initially stagnant liquid. We take advantage of the symmetry of the growth and consider the problem to be axisymmetric. Ten physical variables are involved in describing the hydrodynamics of microlayer formation: liquid and vapor viscosities, μ_l and μ_v, respectively; liquid and vapor densities, ρ_l and ρ_v, respectively; surface tension, σ; bubble growth rate, U_b, the velocity at which the liquid/vapor interface moves inside the surrounding liquid; microscopic contact angle between the liquid vapor interface and the wall at a given reference length scale dx, the minimal mesh size, θ; radial distance from bubble root, r; time, t; and the unknown local thickness of the liquid microlayer forming at the wall, δ. Altogether, these ten variables involve three physical dimensions, and seven dimensionless Pi-groups can fully describe microlayer formation. The proposed dimensionless Pi-groups are:

$$\Pi_1 = \delta/r_c = \delta^*$$
$$\Pi_2 = \mu_l/\mu_v = \mu^*$$
$$\Pi_3 = \rho_l/\rho_v = \rho^*$$
$$\Pi_4 = r/r_c = r^*$$
$$\Pi_5 = t/t_c = t^*$$
$$\Pi_6 = \theta$$
$$\Pi_7 = Ca = \mu_l U_b/\sigma$$

where the reference length and time scales r_c and t_c were defined as follows:

$$r_c = \mu_l/(\rho_l U_b) \tag{1}$$

$$t_c = r_c/U_b = \mu_l/(\rho_l U_b^2) \tag{2}$$

with r_c based on Reynolds number $Re = 1$, for which inertia of the liquid surrounding the bubble and viscous forces at the wall would be comparable. A unique functional form describes the microlayer shape δ^* as a function of the six other Pi-groups, which can be written as follows:

$$\delta^* = f(\mu^*, \rho^*, r^*, t^*, Ca, \theta) \tag{3}$$

In this study we have performed numerical simulations of microlayer formation to quantify f (Eq. (3)). The relevant parameter space for liquid water boiling in lab and industrial conditions (Pressurized Water Reactors, or PWR) is as follows: $\mu_l/\mu_v \in [3.2; 23.3]$, $\rho_l/\rho_v \in [5.9; 1650]$, $Ca \in [0.001; 0.1]$, $\theta \in [0; 90°]$. The range of capillary number, Ca, is obtained from water properties at saturation (μ_l and σ) for both pressures (0.101 MPa and 15.5 MPa), and estimates of bubble growth rates U_b from [50], including a range of cavity mouth radius r_b:

$$U_b = \sqrt{\pi h_{fg} \rho_v \Delta T_{sat}/(7\rho_l T_{sat})} \tag{4}$$

where ΔT_{sat} is the so-called wall superheat at the inception of boiling:

$$\Delta T_{sat} = 2\sigma T_{sat}/(r_b \rho_v h_{fg}) \tag{5}$$

with T_{sat} the saturation temperature, and h_{fg} the latent heat of vaporization. In practice, bubble growth rate U_b and wall superheat ΔT_{sat}, estimated using Eqs. (4) and (5), ought to be experimentally measured.

3. Computational framework

A myriad of methods are available today to simulate two phase flows while tracking the interface between two fluids - see recent review by [51]. The Volume-Of-Fluid (VOF) method, see [52], tracks the interface using a color function C that represents the volume fraction of one phase in each cell of the computational domain. Starting from an initial distribution, the color function C is then advected by the flow:

$$\partial C\rho/\partial t + \nabla \cdot (C\rho \vec{U}) = S_v \tag{6}$$

The Gerris code by [43] solves the incompressible Navier–Stokes equations, and implements the Volume-of-Fluid (VOF) approach for tracking topological changes of the interface:

$$\rho(\partial \vec{U}/\partial t + \vec{U} \cdot \nabla \vec{U}) = -\nabla p + \nabla \cdot (2\mu \bar{\bar{D}}) + \sigma \kappa \delta_s \vec{n} + \vec{F}_{external} \tag{7}$$

$$\partial \rho/\partial t + \nabla \cdot (\rho \vec{U}) = S_v \tag{8}$$

where S_v is a volume source such that $\nabla \cdot \vec{U} = S_v$; $\vec{U}$ is the velocity field; p is the pressure; κ is the curvature of the liquid vapor interface; $\vec{n}$ is the unit vector normal to the liquid vapor interface; $\bar{\bar{D}}$ is

the rate of strain $\bar{\bar{D}} = \frac{1}{2}(\nabla U + (\nabla U)^T)$; ρ is the fluid density, $\rho = C\rho_l + (1 - C)\rho_v$; μ is the fluid viscosity, $\mu = C\mu_l + (1 - C)\mu_v$. A height function method is used for the accurate computation of interface curvature and normals, which together with a balanced-force Continuum Surface Force (CSF) implementation yield a consistent and accurate representation of the surface tension force. The domain is discretized adaptively using the quadtree (in an axisymmetric geometry) finite volumes. The flow equations are discretized using a projection method based on a fractional-step for variable densities. In the projection method, an interim velocity is computed first; this velocity field is projected onto a divergence-free velocity field, with the pressure field obtained as the solution of a Poisson equation. Advection terms are discretized using a second-order upwind scheme. As the face-centered velocities are exactly divergence-free, the volume fractions are advected using these velocities [43,53,54].

The computational domain in Gerris is spatially discretized using a quad mesh, which allows refining specific regions in space while coarsening others. In this work, we typically refine in the vicinity of the wall and at the interface to resolve microlayer formation, while coarsening away from the wall and the bubble interface where such refinement is not necessary. We include a time-dependent volumetric source of vapor within the vapor phase to reproduce the growth observed in lab experiments. The source of vapor fuels bubble growth uniformly inside the bubble, and pushes the liquid vapor interface at the desired rate U_b, hence reproducing the hydrodynamics of hemispherical bubble growth. A time-dependent source is necessary to reproduce the sustained growth of the bubble as its volume increases. For a given constant bubble growth rate U_b ($U_b = dR_b/dt$) during the initial inertia-controlled phase of bubble growth, one can compute the volumetric growth rate dV_b/dt of the equivalent hemispherical bubble as follows:

$$dV_b/dt = 2\pi R_b^2(dR_b/dt) = 2\pi R_b^2 U_b \tag{9}$$

The rate of change of the equivalent hemispherical bubble dV_b/dt is obtained by imposing a volumetric source term S_v in the vapor phase of volume V_b:

$$S_v V_b = dV_b/dt \tag{10}$$

Rearranging Eq. (10), we obtain an explicit expression for the volumetric source term S_v to impose in the vapor phase:

$$S_v = (dV_b/dt)/V_b = 3U_b/(R_{b,0} + U_b t) \tag{11}$$

Note the volumetric source term S_v is uniform in space within the vapor phase at all times, yet time dependent, and function of three parameters: the bubble growth rate U_b known from experiments or derived from Mikic's theory, see Eq. (4), the initial bubble radius $R_{b,0}$ prescribed during the initialization of the numerical simulation, and the physical time t. We typically simulate the growth of the bubble outside of the cavity, and initialize the bubble radius $R_{b,0}$ as the cavity mouth radius r_b (see Eq. (5)).

3.1. Method verification

We verify the implementation of the volumetric source term in axisymmetric configuration in Gerris in the absence of a wall, for the special case of a spherical bubble growth in a (semi)-infinite medium. We compare the volume and shape of the bubble to its simple analytical and spherical reference, and confirm convergence with grid size.

We also verify the convergence of the proposed method in the presence of a wall - see Fig. 3. Two figures of merit are considered: the shape of the liquid microlayer forming at the wall, and the macroscopic bubble growth rate obtained from imposing the
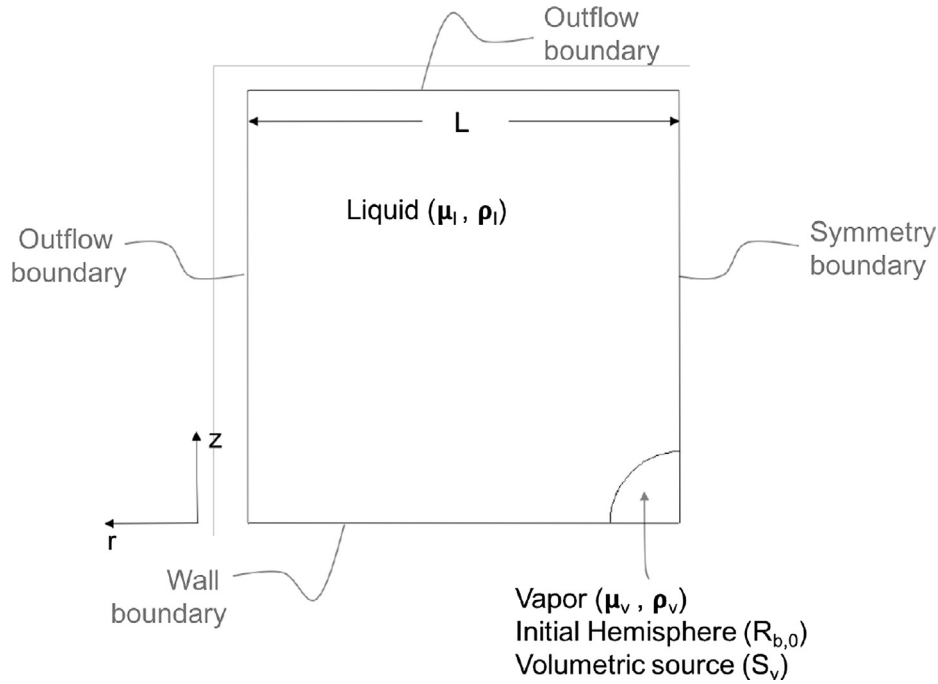
Fig. 3. Computational domain for implementing a volumetric source of vapor to control the growth of the bubble in the presence of a wall.
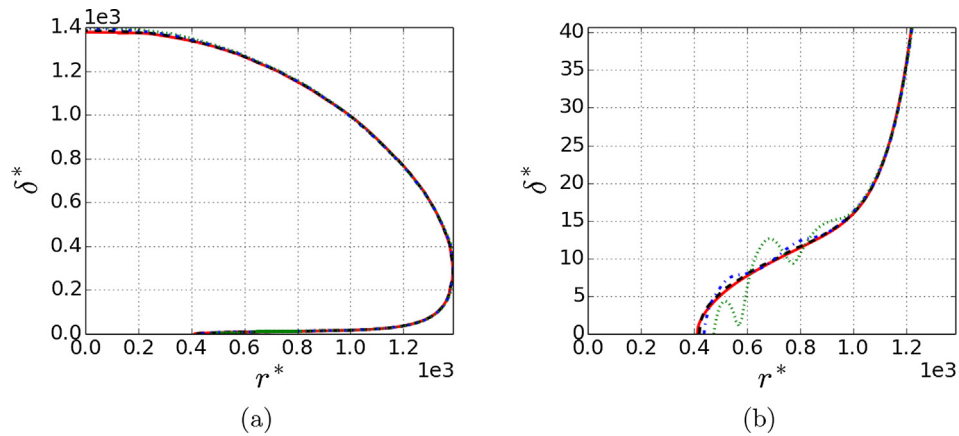

Fig. 4. Axisymmetric shapes of the macroscopic bubble (a) and liquid microlayer (b) obtained in four simulations of bubble growth at a wall, with increased refinement $dx^* = 1$ (⋯), $dx^* = 1/2$ (– ⋅), $dx^* = 1/4$ (- -), $dx^* = 1/8$ (—), in the band: $0 \leqslant \delta^* \leqslant 160$ at the wall, while the refinement elsewhere at the interface is kept identical: $dx^* = 4$, with $R_{b,0}^* = 40$ and $r_c = 0.025$ μm.

volumetric source of vapor inside the bubble. Four simulations of bubble growth at the wall are reported here, with increased refinement in the microlayer region: $dx^* \in \{1, 1/2, 1/4, 1/8\}$, with $dx^* = dx/r_c$, in the band: $0 \leqslant \delta^* \leqslant 160$ at the wall, while the refinement elsewhere at the interface is kept identical: $dx^* = 4$. All four simulations yield identical macroscopic bubbles shapes - see Fig. 4 (a). In Fig. 4(b), the microlayer shape converges to a single profile as we refine the mesh in the microlayer region, from $dx = 250$ nm down to 125 nm, 62.5 nm, and 31.25 nm.

4. Numerical simulation results

Four regions (and scales) can be identified based on the curvature of the bubble interface, see Fig. 5: (i) the contact line region where the interface meets the wall (negative curvature), (ii) the central region of the liquid microlayer ($\approx$ zero curvature), (iii) the microlayer outer-edge region that connects the central region

with the macroscopic bubble cap (up to the bubble nose where the curvature peaks), and (iv) the macroscopic hemispherical bubble cap (uniform curvature along the interface).

4.1. Reducing the parameter space

We perform simulations with all four bounding values for both viscosity and density ratios, and we note the weak dependence of the microlayer shape within both ranges of interest. This weak dependance is supported by the argument that the properties of the liquid phase affect the hydrodynamics of this problem much more than those of the vapor phase, which in practice can be considered as an inviscid and massless fluid. Therefore, in the rest of the study, we will no longer consider the dependence of the microlayer formation on the viscosity and density ratios, which simplifies the function in Eq. (3) for the conditions of interest.
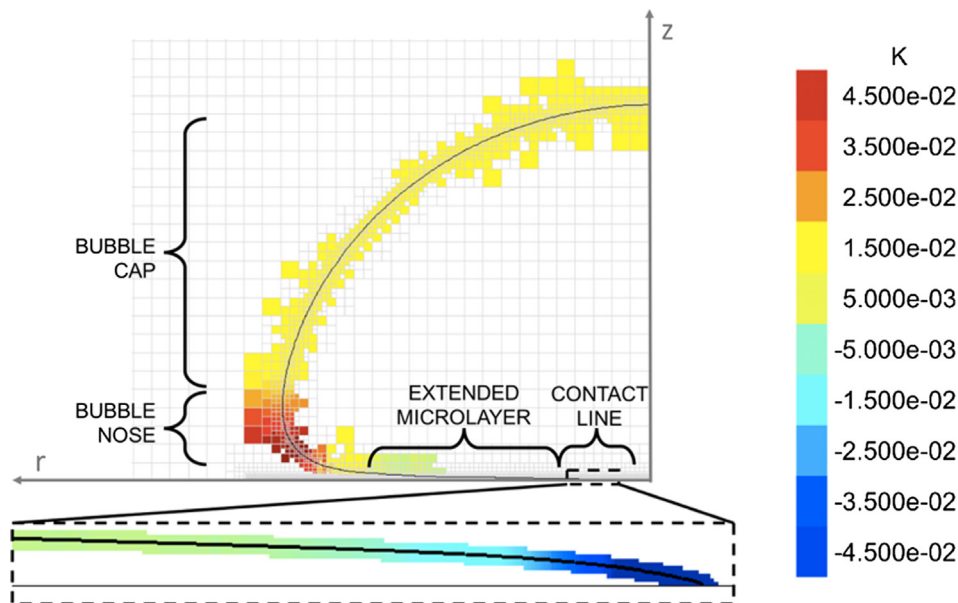
Fig. 5. Typical axisymmetric shape of a growing bubble at a wall. Interface is solid black line. Curvature κ is given by the colormap: blue in the contact line region is negative curvature (minimum reached at the contact point $\kappa = -6.6 \times 10^{-1}$ [1/μm]), green in the central linear region is approaching zero curvature ($\kappa \approx 10^{-3}$ [1/μm]), red at the bubble nose is maximum curvature ($\kappa = 5.8 \times 10^{-2}$ [1/μm]), and yellow is the uniform curvature along the interface at the bubble cap as the bubble grows hemispherically ($\kappa \approx 1.5 \times 10^{-2}$ [1/μm]). The range used in the color map does not reflect the maximum positive value and minimum negative value taken by the curvature, but rather is centered around 0 to allow easier identification of all four regions, also denoted in the image with direct labeling. (For interpretation of the references to colour in this figure legend, the reader is referred to the web version of this article.)

4.2. Modeling the microlayer inner edge

A general model of moving contact lines is out of the scope for the present paper. However, we identify multiple scenarios that could take place at the inner edge of the microlayer, where the liquid/vapor interface meets the solid surface: (i) no motion of the contact line, pinned either at the cavity mouth or elsewhere on the wall surface, (ii) intermittent motion of the contact line, where pinning and depinning of the contact line occurs at the wall, and (iii) continuous motion of the contact line, that could be described by a mobility law $\theta = g(Ca_{cl})$, with Ca_{cl} the capillary number associated with the motion of the contact line, and θ the contact angle. When the contact line is free to move (no pinning), its motion relative to the bubble growth dictates whether a microlayer forms at the wall or not.

Qualitatively, the radial component of the surface tension force applied to a liquid wedge decreases in magnitude for increasing contact angles. Hence the contact line is expected to move faster at higher contact angles and the wetted fraction underneath the bubble is expected to be reduced at higher contact angles. Quantitatively, physical models or experimental data on contact line motion are needed to conclude on whether a microlayer is expected to form or not, for a given fluid/solid pair and surface condition, which cannot be resolved by the Gerris flow solver alone. In this work, we simulate moving contact lines for a wide range of constant and uniform contact angles at the wall, ranging from 10° to 90°. An extension of this work could include a physical mobility law to apply the proposed methodology to a specific application for which the physical motion of the contact line is known.

The simulation of moving contact lines is made possible with Gerris through the use of a height-function based model of contact angle implemented by [55], where a numerical contact angle θ is imposed in the cell at the wall containing the contact line. This microscopic contact angle is used to define the normal to the interface at the contact line, and therefore impacts both the computed curvature and the resulting surface tension force at the contact line. Cell normal velocities are used to advect volume fractions, resulting in an implicit slip along no-slip boundaries such as along the wall, which allows the contact line to move at the wall with the prescribed microscopic contact angle θ. As a consequence, the dynamics of the simulated moving contact line depend both on the microscopic contact angle prescribed and on grid size. Specific mesh convergence studies are reported in other papers, including most recently in [48].

Typical simulation results are shown in Fig. 6: we confirm that the wetted fraction underneath the bubble is reduced for higher contact angles, and we note the formation of a bulge of liquid at the inner edge of the microlayer. Bulge formation at higher contact angles is specifically discussed in a separate paper [48], where we focus on the problem of forced dewetting transition for a wide range of contact angles using direct numerical simulations. In
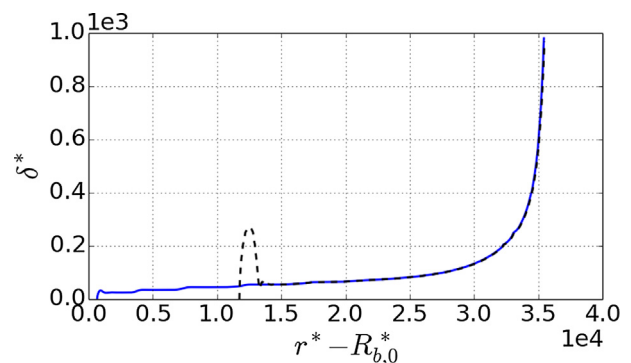

Fig. 6. Microlayer thickness profiles δ^* for two contact angles $\theta = 20°$ (blue solid line) and $\theta = 80°$ (black dashed line), as a function of dimensionless radial distance $r^* - R_{b,0}^*$. $Ca = 0.1$, $t^* = 3.6 \times 10^3$ ($r_c = 10$ nm, $t_c = 1$ ns). (For interpretation of the references to colour in this figure legend, the reader is referred to the web version of this article.)

particular, we provide a numerical dataset for the critical capillary number Ca_{cr} at which the dewetting transition occurs, as a function of the mesh size Δ, and contact angle θ_Δ ranging from 15° to 110°.

At the inner edge of the microlayer, the surface tension force acts against the viscous force at the wall and pushes the contact line outwards, similar to the classic hole expansion problem, see [56–60]. The Ohnesorge number Oh is defined as:

$$Oh = \mu_l / \sqrt{\delta \rho_l \sigma} = \sqrt{Ca/\delta^*}$$

Three regimes are identified based on the Ohnesorge number: $Oh < 0.1$, $Oh \in [0.1; 10]$, and $Oh > 10$. As Oh increases, the capillary waves found at the tip disappear through the action of viscosity. In all simulations presented in this paper, we find that Oh ranges from 0.001 to 0.1, which corresponds to the first regime where capillary waves are expected in the vicinity of the tip, and damped away from the tip due to viscous effects, leaving the rest of the extended liquid layer unaffected by the motion of the bulge, as confirmed in Fig. 6.

The microscopic contact angle θ used in Gerris allows us to represent the behavior of the moving contact line as a boundary condition, or subgrid model, without attempting to resolve the complex physics at play at the scale of the contact line. For simplicity in the rest of the paper, we present results for low microscopic contact angles in order to observe microlayer formation. However, the informed reader would need to consider the specific motion of the contact line for the wall condition and solid/fluid pair of interest in order to determine whether a microlayer forms or not in such conditions, and quantify the relative motion of the contact line with respect to the macroscopic bubble.

4.3. Modeling the microlayer central region

An analytical model for microlayer formation has been proposed by [49]:

$$\delta = C_0 \sqrt{v_l t_g} \tag{12}$$

where t_g is the growth time, C_0 a dimensionless constant, and $v_l = \mu_l/\rho_l$. Interestingly, the analytical model in [49] was formulated under the assumption of the diffusion-controlled growth period during which $R_b \sim \sqrt{t}$. In this work, we focus on the inertia-controlled growth period, during which $R_b \sim t$. Using classic boundary layer theory, inertia and viscous forces of the same order yields:

$$\left(\frac{R_b}{\delta}\right)^2 / Re \sim 1 \tag{13}$$

with $Re = \frac{U_b R_b}{v_l}$. Assuming constant bubble growth rate U_b, $R_b \sim U_b t$ yields:

$$\delta \sim R_b / \sqrt{U_b R_b / v_l} \tag{14}$$

which rearranges to:

$$\delta \sim \sqrt{v_l t} \tag{15}$$

Using C_0 to denote a dimensionless constant, and considering the constant bubble growth rate U_b, we obtain the dimensionless form:

$$\delta^* = C_0 \sqrt{(\mu_l/\rho_l) * (r/U_b)} = C_0 \sqrt{r^*} \tag{16}$$

With an initial bubble dimensionless radius $R_{b,0}^*$, and assuming that the contact line is either pinned at its initial position ($r^* = R_{b,0}^*$) or that its outward motion is negligible compared to the macroscopic bubble growth, then the square root model becomes:

$$\delta^* = C_0 \sqrt{r^* - R_{b,0}^*} \tag{17}$$

We present in Fig. 7 the square root model along with our numerical simulation results, for the range of capillary numbers of interest, $Ca \in [0.001; 0.1]$, and for a low contact angle $\theta = 10°$ for which we observe the formation of the microlayer with negligible motion of the contact line compared to the radial extension of the bubble growth. Numerical simulations at higher contact angles were also performed for sake of generality, with contact angles ranging from 10° to 90°. As long as a microlayer forms, higher contact angle conditions yield identical microlayer profiles away from the contact line region, and do not affect the overall volume of liquid trapped underneath the bubble, as shown in the previous section and in Fig. 6.

More specifically, we plot the simulated microlayer profiles δ^* as a function of dimensionless radial distance $r^* - R_{b,0}^*$ on the left panels of Fig. 7, for three consecutive times, and for capillary numbers spanning the range of interest: $Ca = 0.001$ (a), $Ca = 0.01$ (c) and $Ca = 0.1$ (e). We note that the microlayer continuously grows over time, and that the portion of the thickness profile that has already formed at a given time remains unchanged at later times, with the exception of the contact line region where the dewetting process increases liquid build-up over time in the bulge.

The volume of liquid V_{in} in the bulge is typically negligible compared to the total volume of liquid V_{tot} trapped under the bubble ($V_{in}/V_{tot} < 0.1\%$), and will not be modeled in the later portion of the paper. This simplification only applies if the contact line's outward motion is negligible compared to the bubble growth, which depends on the physical behavior of the contact line for a given fluid/solid pair and surface condition. In our numerical simulations, and for the contact angle model described earlier, we note in [61] that the simplification breaks down for very low capillary numbers ($Ca \to 0$) and large contact angles ($\theta \to 90°$), where the velocity of the contact line approaches the bubble growth rate, and no microlayer is left behind.

In Fig. 7(b), (d) and (f), we plot the ratio $\delta^*/\sqrt{r^* - R_{b,0}^*}$ as a function of dimensionless radial distance $r^* - R_{b,0}^*$. We note that the ratio is constant in the central region of the microlayer, and that the magnitude of the ratio is close to 0.5 for all the considered capillary numbers. From this observation, we use $C_0 = 0.5$ in the square root model prediction, and compare it with our simulation results in Figs. 8–10, for various times and Ca of interests.

Modeling microlayer formation is particularly important to capture two key boiling characteristics: (i) the wall heat flux and (ii) the total volume of liquid trapped underneath the bubble that evaporates and that fuels bubble growth up to its departure from the heated surface. The square root model is able to capture both thickness and volume of the microlayer in the central region, which corresponds to the thin part of the microlayer.

We also conclude from Figs. 8–10 that the square root model does not capture the outer-edge region of the microlayer, and therefore the total volume of liquid trapped underneath the bubble is underestimated. This conclusion suggests the need for specific modeling of the transition from the central (thin) region of near-zero curvature, to the outer-edge (thick) region, of non-zero curvature which is left for future work.

4.4. Validating numerical results with experimental data and existing models

Initially in [49], experimental data on organic liquids boiling at low pressures provided estimates of C_0, in the range of 0.5 to 1.0, for which experimental data and square root model were found to agree within ±25%.

Recent advances in microlayer thickness measurements at different radial locations and short time scales by [35] uncovered

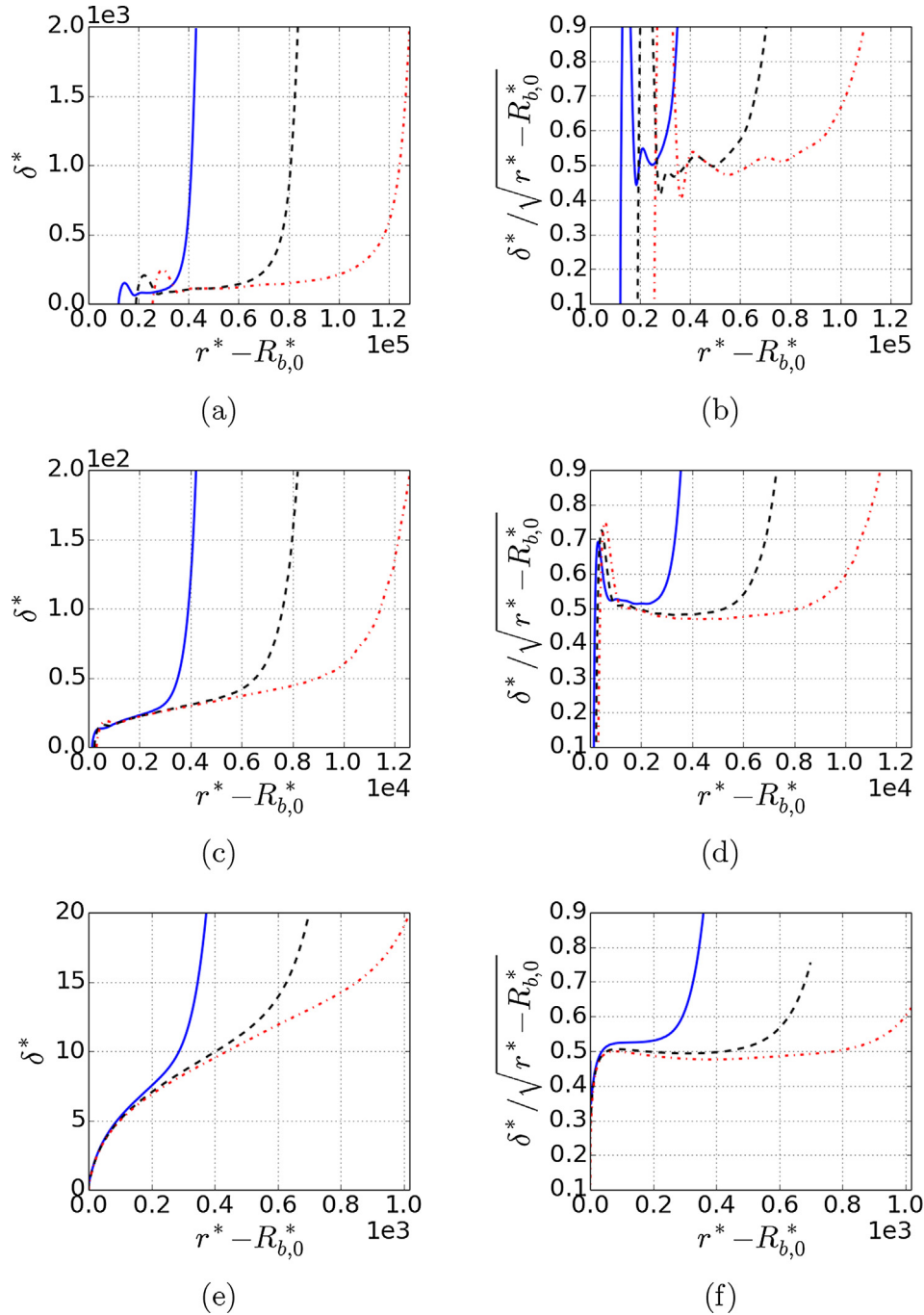**Fig. 7.** Microlayer dimensionless profiles δ^* plotted in left column: (a), (c), and (e), and ratios $\delta^*/\sqrt{r^* - R_{b,0}^*}$ plotted in right column: (b), (d), and (f), as a function of dimensionless radial distance $r^* - R_{b,0}^*$, with $R_{b,0}^*$ the initial dimensionless bubble radius. Each row corresponds to a different Ca number: $Ca = 0.001$ in top row (a) and (b), $Ca = 0.01$ in middle row (c) and (d), $Ca = 0.1$ in bottom row (e) and (f). Microscopic contact angle is $\theta = 10°$, and finest mesh size at the wall is 31.25 nm. Same physical times are plotted in all panels: $t = 10$ μs (blue solid line), $t = 20$ μs (black dashed line), $t = 30$ μs (red dot-dashed line). In each row, the following characteristic length and time scales are imposed: $(r_c = 1$ nm, $t_c = 1$ ns) in top row (a) and (b), $(r_c = 10$ nm, $t_c = 10$ ns) in middle row (c) and (d), $(r_c = 0.1$ μm, $t_c = 0.1$ μs) in bottom row (e) and (f). (For interpretation of the references to colour in this figure legend, the reader is referred to the web version of this article.)

two regimes based on a modified Bond number $\hat{Bo}$:

$$\hat{Bo} < 13 : C_{exp} = 0.13 Bo^{0.38} \tag{18}$$

$$\hat{Bo} \geqslant 13 : C_{exp} = 0.34 \tag{19}$$

with $\hat{Bo} = \rho_l r^2 U / t\sigma$, and C_{exp} the experimental measurement of C_0. Rearranging $\hat{Bo}$ we obtain $\hat{Bo} = \rho_l U^2 tU/\sigma = t^*/Ca$. The transition at $\hat{Bo} = 13$ correspond to physical times $t = \hat{Bo} Ca t_c$ in the range of

10^{-3} μs to 10^{-1} μs for the case of boiling water at 0.101 MPa ($Ca \in [0.001; 0.1]$, and $t_c \sim 0.1$ μs). Therefore, only the second regime is relevant to microlayer formation, which occurs over tens of μs, and we note $C_{exp} = 0.34$ the corresponding experimental measurement of C_0 from [35], which is of the same order of magnitude as the value of 0.5 we obtain in our numerical simulations.

Lastly, we use experimental measurements of microlayer thickness to validate our numerical results, for the case of water at saturation at 0.101 MPa (data courtesy of Prof. Hyungdae Kim). In the
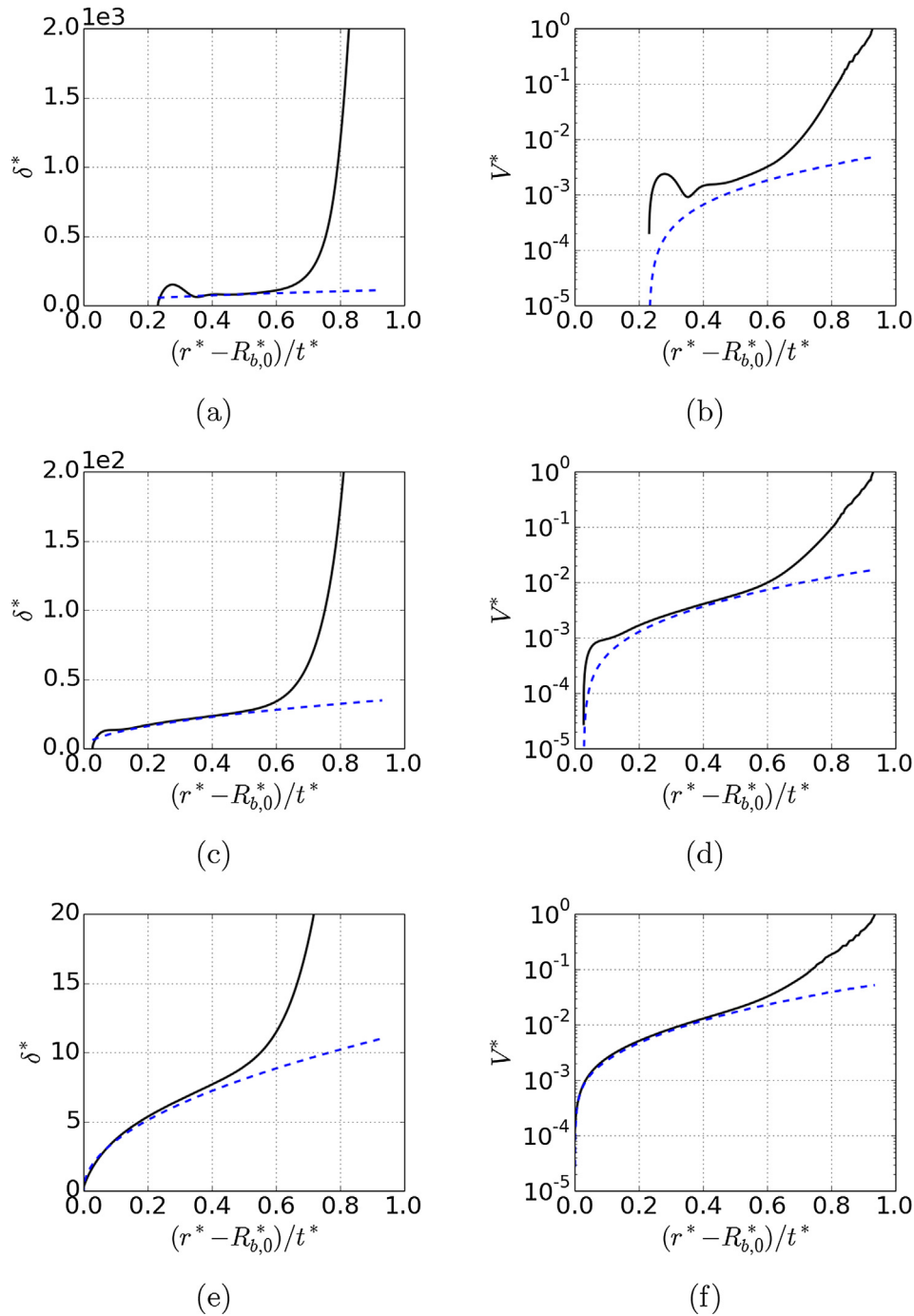
Fig. 8. Microlayer dimensionless profiles δ^* (left column) and subsequent volume V^* (right column) with $V^* = V/V_{tot}$, where V_{tot} is the total volume of liquid trapped underneath the bubble, as a function of dimensionless radial extension $(r^* - R_{b,0}^*)/t^*$, from simulations (black solid line), and from the square root model: $\delta^* = 0.5\sqrt{r^* - R_{b,0}^*}$ (blue dashed line). $Ca = 0.001$ (top row), $Ca = 0.01$ (middle row), $Ca = 0.1$ (bottom row). Physical time $t = 10\,\mu s$. (For interpretation of the references to colour in this figure legend, the reader is referred to the web version of this article.)

experiment, a high-speed video camera was used to measure bubble radius over time, and an IR camera was used to measure the wall temperature distribution underneath the bubble. From the bubble height and width measurements shown in Fig. 2, we conclude that the bubble grew hemispherically. An additional high-speed video camera was used to measure microlayer thickness. The measurement error was assessed using a solid convex lens of known curvature: the error in thickness measurement is found to be $\sim 10\%$ for thicknesses greater than $0.5\,\mu m$, and $\sim 30\%$ otherwise. The earliest bubble growth rate was measured at $t = 20\,\mu s$, see in Fig. 11, and drops dramatically at early times

which indicates that the initial bubble growth rate during the first tens of μs may have been much higher than its first available measured value of $4.2\,m/s$. We include this uncertainty in initial bubble growth rates in our validation below through a sensitivity study on the initial bubble growth rate: in blue, we assume the bubble growth rate to be constant during the first $20\,\mu s$, and in red we assume its acceleration to be constant during the first $20\,\mu s$.

We compare our numerical results against experimental results in Fig. 11(b): black squares represent the earliest experimental measurement of the microlayer thickness, which took place at time
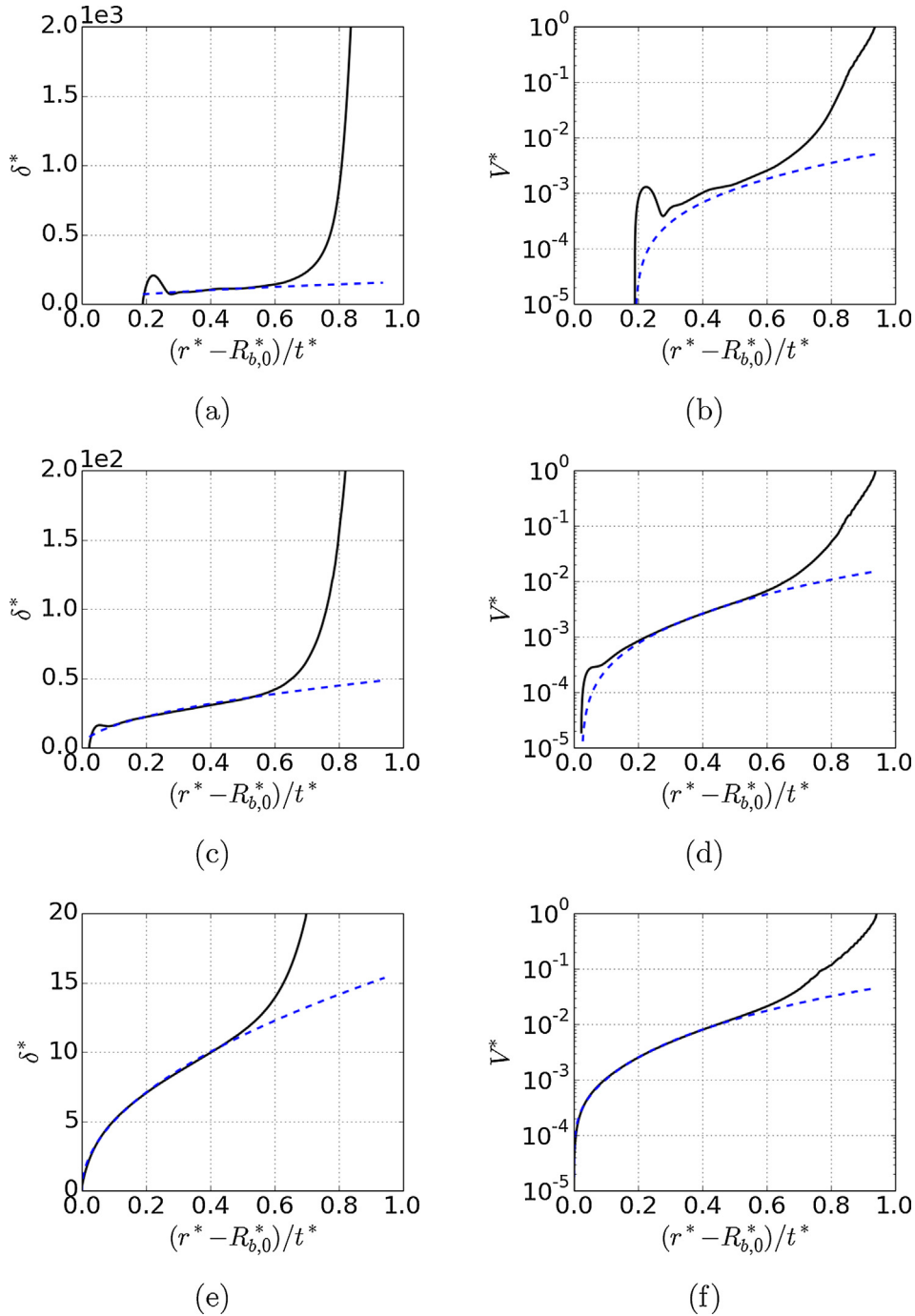
Fig. 9. Microlayer dimensionless profiles δ^* (left column) and subsequent volume V^* (right column) with $V^* = V/V_{tot}$, where V_{tot} is the total volume of liquid trapped underneath the bubble, as a function of dimensionless radial extension $(r^* - R_{b,0}^*)/t^*$, from simulations (black solid line), and from the square root model: $\delta^* = 0.5\sqrt{r^* - R_{b,0}^*}$ (blue dashed line). $Ca = 0.001$ (top row), $Ca = 0.01$ (middle row), $Ca = 0.1$ (bottom row). Physical time $t = 20$ μs. (For interpretation of the references to colour in this figure legend, the reader is referred to the web version of this article.)

$t = 410$ μs; and grey triangles are obtained by deducing the microlayer thickness at $t = 20$ μs, assuming that the heat transfer within the microlayer is purely by conduction, see [10]:

$$\frac{\partial \delta(r,t)}{\partial t} = -\frac{k_l \Delta T_{sat}(r,t)}{\rho_l h_{fg} \delta} \tag{20}$$

with k_l the liquid thermal conductivity, ΔT_{sat} the local and time-dependent wall superheat, ρ_l the density of the liquid and h_{fg} the latent heat of vaporization. To simplify the calculation of this estimate, we assume constant wall superheat:

$$\Delta T_{sat}(r,t) = \Delta T_{sat,0}$$

for which a closed form exists:

$$\delta(r,t_0) = \sqrt{\delta(r,t_1)^2 + \frac{2k_l \Delta T_{sat,0}}{\rho_l h_{fg}}(t_1 - t_0)} \tag{21}$$

with $t_0 = 20$ μs, $t_1 = 410$ μs and $\Delta T_{sat,0} = 11.7\,°C$ in our case. Assuming constant wall superheat results in under estimating the thermal coupling with the wall surface, and therefore over
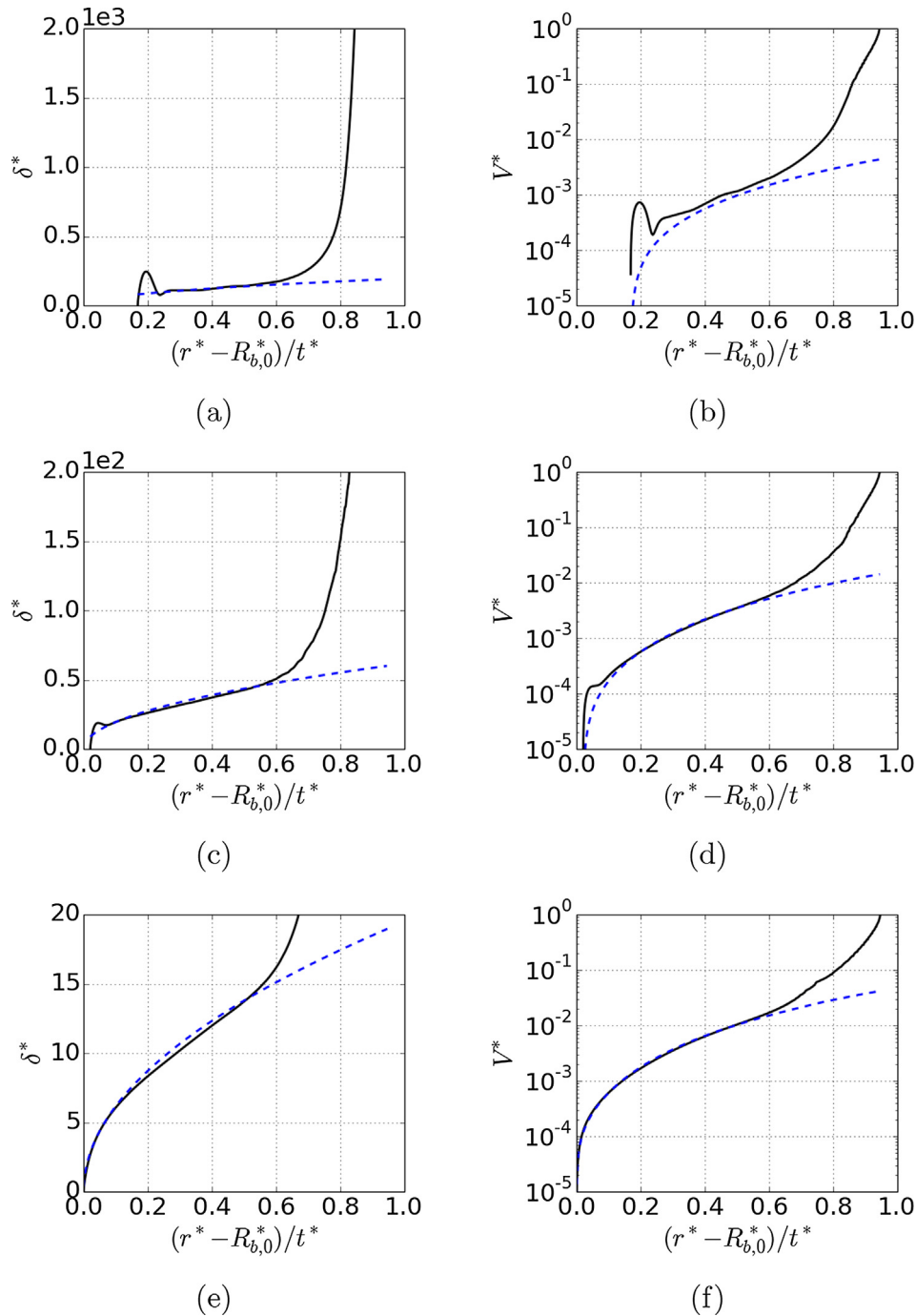
Fig. 10. Microlayer dimensionless profiles δ^* (left column) and subsequent volume V^* (right column) with $V^* = V/V_{tot}$, where V_{tot} is the total volume of liquid trapped underneath the bubble, as a function of dimensionless radial extension $(r^* - R_{b,0}^*)/t^*$, from simulations (black solid line), and from the square root model: $\delta^* = 0.5\sqrt{r^* - R_{b,0}^*}$ (blue dashed line). $Ca = 0.001$ (top row), $Ca = 0.01$ (middle row), $Ca = 0.1$ (bottom row). Physical time $t = 30$ μs. (For interpretation of the references to colour in this figure legend, the reader is referred to the web version of this article.)

estimating the volume of liquid evaporated, in particular in the region of small thickness δ (e.g. low radial distance r).

The comparison in Fig. 11(b) shows a reasonable agreement between modeled and measured microlayer thicknesses at $t = 20$ μs despite the inherent assumptions in the model. We also note a departure from the model in the low thickness region. We expect this discrepancy to be reduced if we no longer assume constant wall superheat, but include the thermal coupling between the microlayer and the heated wall. Such coupling would require to solve for the heat equation in the substrate, while using Eq. (20) as a flux boundary condition at the wall surface, as shown in previous

work by [10]. The initial evaporation of the microlayer would locally reduce the wall superheat and therefore would slow down the rate of evaporation of the microlayer. This slowdown effect of the microlayer evaporation due to conjugate heat transfer with the solid surface is currently not included in Fig. 11(b), and could explain the overestimated values of the microlayer thickness in the low thickness region at $t = 20$ μs. The following properties of water at saturation at 0.101 MPa were used: $\mu_l = 3.5 \times 10^{-4}$ Pa s, $\rho_l = 950$ kg/m³. The first measured value of bubble growth rate was $U_b(t \sim 20$ μs$) \sim 4.2$ m/s.
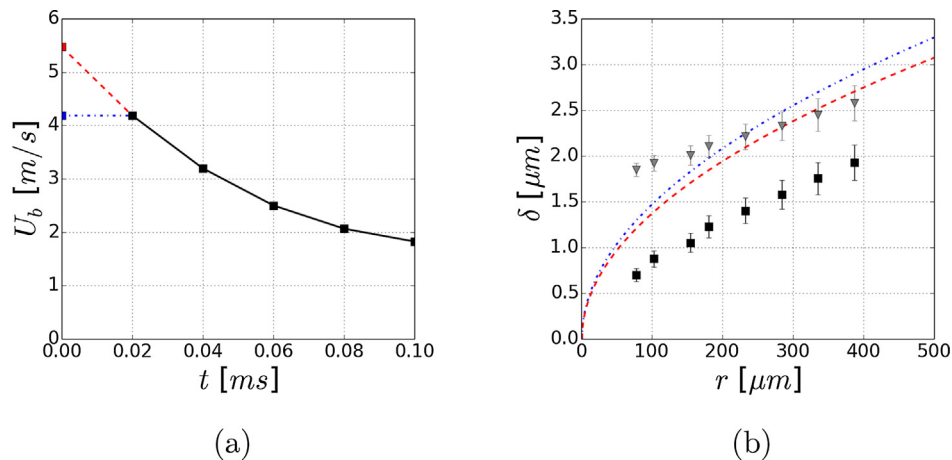
Fig. 11. Measured bubble growth rates (black squares) over time (a), and two assumed initial regimes: constant growth rate (blue dash-dotted line), or constant acceleration (red dashed line). Thickness δ (in μm) measured in lab experiment (black squares) of boiling water at saturation at 0.101 MPa, 0.41 ms after boiling inception (b). The deduced microlayer thickness at $t = 20$ μs (grey triangles) is obtained assuming that the heat transfer within the microlayer is purely by conduction. The wall temperature at boiling inception is 111.7 °C, and the wall heat flux is 209 kW/m² (courtesy of Prof. Hyungdae Kim). Predictions from the square root model are plotted for the two initial profiles of U_b showed in (a). The first measured value of U_b is $U_b(t \sim 20$ μs$) \sim 4.2$ m/s. (For interpretation of the references to colour in this figure legend, the reader is referred to the web version of this article.)
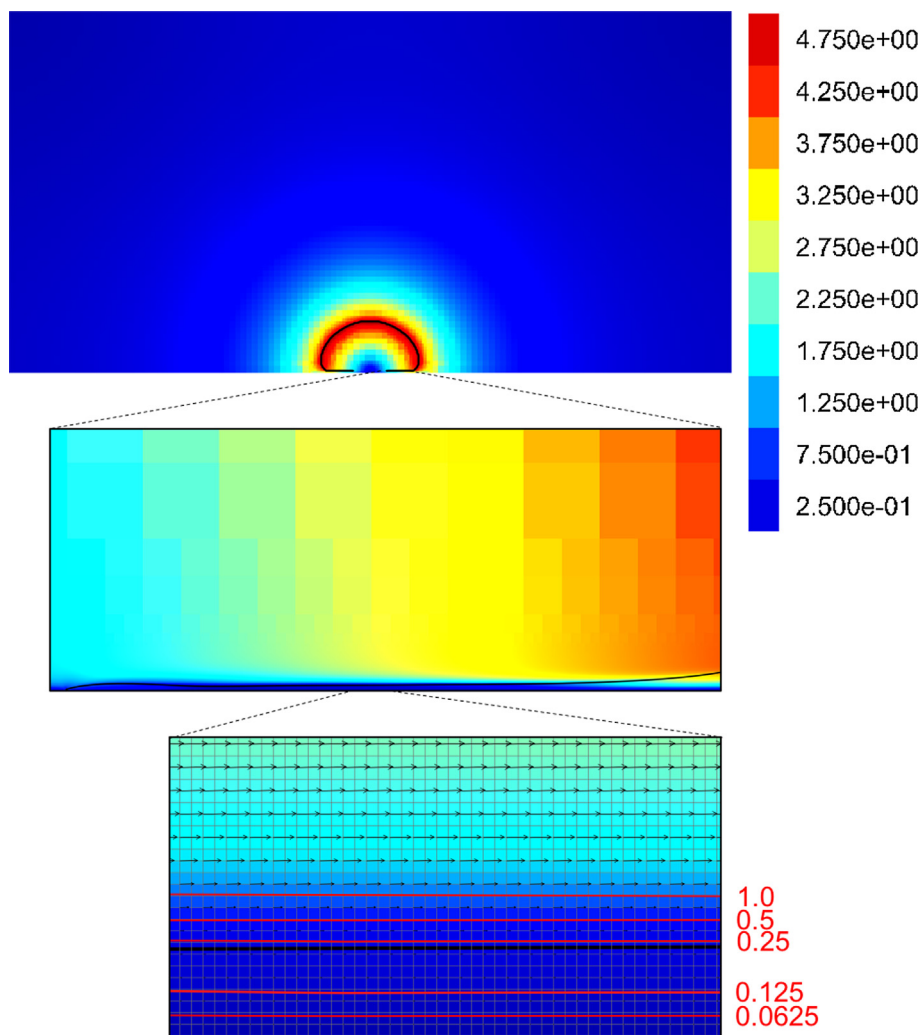

Fig. 12. Norm of the velocity field in the computational domain for $Ca = 0.009$, $t^* = 6.2 \times 10^3$, $\theta = 20°$, at the scale of the bubble (top), at the scale of the extended microlayer (middle), and at the scale of the microlayer (bottom), and ranges from 0 [m/s] (dark blue) to $U_b = 5$ [m/s] (dark red). Red isolines (bottom) of velocity norm of 0.0625, 0.125, 0.25, 0.5 and 1.0 [m/s] are also provided for reference. The liquid/vapor interface is in black. The mesh is shown in the bottom figure for reference, as well as the velocity field (black arrows). Negligible flow is reported in the microlayer. (For interpretation of the references to colour in this figure legend, the reader is referred to the web version of this article.)

Lastly, we confirm in Fig. 12 that there is negligible flow in the microlayer for the representative example of $Ca = 0.009$, $t^* = 6.2 \times 10^3$, $\theta = 20°$. Isolines of velocity norm are included in the bottom insert of Fig. 12, and reveal that the norm of the velocity field in the microlayer ranges between 0 and 0.25 m/s, over 20 times lower than the characteristic velocity U_b.

5. Summary and conclusions

In this work, we used Computational Fluid Dynamics with Interface Tracking Methods to numerically reproduce the hydrodynamics of bubble growth at a wall, and resolve the formation of the liquid microlayer at the wall with high resolution in space and time. We identified the minimum set of dimensionless parameters that controls microlayer formation, and reduced the parameter space for the conditions and fluid of interest, namely water at pressures ranging from 0.101 MPa (lab conditions) and up to 15.5 MPa (reactor conditions):

$$\delta^* = f(r^*, t^*, Ca, \theta) \tag{22}$$

with δ^* the shape of the extended liquid microlayer, $r_c = \mu_l/(\rho_l U_b)$ and $t_c = r_c/U_b$ the characteristic length and time scales used, respectively. The fluid analyzed in this study is water, however because of the use of dimensionless parameters, the results presented here are broadly applicable to other fluids with dimensionless parameters within the same ranges.

We found that three regions need to be modeled in order to accurately represent the thickness of the microlayer, and the total volume of liquid trapped underneath the bubble:

1. the inner region: our qualitative results confirm that the dynamics of the moving contact line at the inner edge of the microlayer dictate whether a microlayer forms or not. The proposed methodology can be used to include a physical mobility law in place of the current static microscopic contact angle used, and simulate the liquid build-up at the inner edge for a given fluid/solid pair and surface conditions for which the motion of the contact line is known.
2. the central region: our simulation results indicate that the square root model initially proposed by [49] captures the central region of the microlayer accurately in the case of hemispherical bubble growth:

$$\delta^* \approx 0.5 \sqrt{r^* - R_{b,0}^*} \tag{23}$$

as long as the motion of the contact line is negligible compared to the bubble growth rate. In addition, we benchmark our results against the earliest microlayer thickness measurements available (courtesy of Prof. Hyungdae Kim). A reasonable agreement between modeled and measured microlayer thicknesses is obtained despite the inherent assumptions in the model.
3. the outer region: we note that the square root model breaks down at the microlayer outer-edge, where its curvature rapidly increases to meet the non-zero curvature of the bubble cap. Specific modeling of this transition region, denoted Region IV in Fig. 1, is left for future work.

These results clarify the remaining steps needed to build a general model on microlayer formation that resolves the initial and rapid phase of bubble growth in nucleate boiling, called inertia-controlled phase, which lasts tens of μs in the case of water at atmospheric pressure. The next phase of bubble growth, the thermal diffusion controlled phase, is much slower and lasts tens of milliseconds in the case of water at atmospheric pressure. In practice, the microlayer formation model allows initialization of boiling

simulations at the end of the rapid inertia-controlled phase of bubble growth during which the microlayer forms.

Lastly, we conclude that the numerical methods used in this study have proved to be mature enough to investigate microlayer formation and its parameter space of interest, within reasonable simulation time while achieving sufficiently fine spatial and temporal resolution. However, additional experimental data on moving contact lines and microlayer thickness profiles at very short time and length scales relevant to microlayer formation are still needed to continue to benchmark numerical simulations and unlock potential predicting capabilities.

Conflict of interest

None.

Appendix A. Supplementary material

Supplementary data associated with this article can be found, in the online version, at https://doi.org/10.1016/j.ijheatmasstransfer.2018.06.041.

References

[1] L. Yeh, Review of heat transfer technologies in electronic equipment, Trans. ASME-P-J. Electron. Pack. 117 (4) (1995) 333–339.
[2] R.M. Manglik, On the advancements in boiling, two-phase flow heat transfer, and interfacial phenomena, J. Heat Transfer 128 (12) (2006) 1237–1242.
[3] S.G. Kandlikar, History, advances, and challenges in liquid flow and flow boiling heat transfer in microchannels: a critical review, J. Heat Transfer 134 (3) (2012) 034001.
[4] N. Churaev, The effect of adsorbed layers on van der waals forces in thin liquid films, Coll. Polym. Sci. 253 (2) (1975) 120–126.
[5] J. N. Chung, T. Chen, S. Maroo, A review of recent progress on nano/micro scale nucleate boiling fundamentals, Front. Heat Mass Transf. 2(2), doi:https://doi.org/10.5098/hmt.v2.2.3004.
[6] V. Dhir, Boiling heat transfer, Ann. Rev. Fluid Mech. 30 (1) (1998) 365–401.
[7] P. Stephan, J. Kern, Evaluation of heat and mass transfer phenomena in nucleate boiling, Int. J. Heat Fluid Flow 25 (2) (2004) 140–148.
[8] J. Kim, Review of nucleate pool boiling bubble heat transfer mechanisms, Int. J. Multiph. Flow 35 (12) (2009) 1067–1076.
[9] C. Kunkelmann, P. Stephan, Modification and extension of a standard volume-of-fluid solver for simulating boiling heat transfer, in: Proceedings of the 5th European Conference on Computational Fluid Dynamics ECCOMAS CFD2010, Lisbon, Portugal, 2010.
[10] A. Guion, D. Langewisch, J. Buongiorno, On the liquid microlayer underneath a vapor bubble growing at a heated wall, Int. Conf. Multiph. Flow (2013) 1–13, https://doi.org/10.1115/HT2013-17174.
[11] Y. Jiang, H. Osada, M. Inagaki, N. Horinouchi, Dynamic modeling on bubble growth, detachment and heat transfer for hybrid-scheme computations of nucleate boiling, Int. J. Heat Mass Transf. 56 (1) (2013) 640–652.
[12] S. Jung, H. Kim, An experimental method to simultaneously measure the dynamics and heat transfer associated with a single bubble during nucleate boiling on a horizontal surface, Int. J. Heat Mass Transf. 73 (2014) 365–375.
[13] Y. Sato, B. Niceno, A depletable micro-layer model for nucleate pool boiling, J. Comput. Phys. 300 (2015) 20–52.
[14] G. Giustini, S. Jung, H. Kim, S. Walker, Evaporative thermal resistance and its influence on microscopic bubble growth, Int. J. Heat Mass Transf. 101 (2016) 733–741.
[15] A. Zou, A. Chanana, A. Agrawal, P.C. Wayner Jr., S.C. Maroo, Steady state vapor bubble in pool boiling, Scient. Rep. 6 (2016).
[16] A. Zou, D.P. Singh, S.C. Maroo, Early evaporation of microlayer for boiling heat transfer enhancement, Langmuir 32 (42) (2016) 10808–10814.

[17] S. Jung, H. Kim, Hydrodynamic formation of a microlayer underneath a boiling bubble, Int. J. Heat Mass Transf. 120 (2018) 1229–1240.
[18] A. Urbano, S. Tanguy, G. Huber, C. Colin, Direct numerical simulation of nucleate boiling in micro-layer regime, Int. J. Heat Mass Transf. 123 (2018) 1128–1137.
[19] S. Bankoff, Entrapment of gas in the spreading of a liquid over a rough surface, AIChE J. 4 (1) (1958) 24–26.
[20] F.D. Moore, R.B. Mesler, The measurement of rapid surface temperature fluctuations during nucleate boiling of water, AIChE J. 7 (4) (1961) 620–624.
[21] R. Hendricks, R. Sharp, Initiation of cooling due to bubble growth on a heating surface, NASA Technical Note D-2290, 1964, pp. 1–18.
[22] N.B. Hospeti, R.B. Mesler, Deposits formed beneath bubbles during nucleate boiling of radioactive calcium sulfate solutions, AIChE J. 11 (4) (1965) 662–665.
[23] H. Jawurek, Simultaneous determination of microlayer geometry and bubble growth in nucleate boiling, Int. J. Heat Mass Transf. 12 (8) (1969).
[24] G. Foltz, R. Mesler, The measurement of surface temperatures with platinum films during nucleate boiling of water, AIChE J. 16 (1) (1970) 44–48.
[25] R. Judd, Laser interferometric investigation of the microlayer evaporation phenomenon, J. Heat Transfer (1975) 88–92.
[26] R. Judd, K. Hwang, A comprehensive model for nucleate pool boiling heat transfer including microlayer evaporation, ASME J. Heat Transfer 98 (4) (1976) 623–629.
[27] L. Koffman, M. Plesset, Experimental study of microlayer formed during vapour bubble growth on the heated solid surface, Trans. ASME J. Heat Transf. 105 (1983).
[28] S. Moghaddam, K. Kiger, Physical mechanisms of heat transfer during single bubble nucleate boiling of fc-72 under saturation conditions-i. experimental investigation, Int. J. Heat Mass Transf. 52 (5) (2009) 1284–1294.
[29] I. Golobic, J. Petkovsek, M. Baselj, A. Papez, D. Kenning, Experimental determination of transient wall temperature distributions close to growing vapor bubbles, Heat Mass Transf. 45 (7) (2009) 857–866.
[30] H. Kim, J. Buongiorno, Detection of liquid–vapor–solid triple contact line in two-phase heat transfer phenomena using high-speed infrared thermometry, Int. J. Multiph. Flow 37 (2) (2011) 166–172.
[31] M. Gao, L. Zhang, P. Cheng, X. Quan, An investigation of microlayer beneath nucleation bubble by laser interferometric method, Int. J. Heat Mass Transf. 57 (1) (2013) 183–189.
[32] S. Jung, H. Kim, An experimental study on heat transfer mechanisms in the microlayer using integrated total reflection, laser interferometry and infrared thermometry technique, Heat Transf. Eng. 36 (12) (2015) 1002–1012.
[33] S. Bigham, S. Moghaddam, Role of bubble growth dynamics on microscale heat transfer events in microchannel flow boiling process, Appl. Phys. Lett. 107 (24) (2015) 244103.
[34] T. Yabuki, O. Nakabeppu, Heat transfer mechanisms in isolated bubble boiling of water observed with mems sensor, Int. J. Heat Mass Transf. 76 (2014) 286–297.
[35] T. Yabuki, O. Nakabeppu, Microlayer formation characteristics in pool isolated bubble boiling of water, Heat Mass Transf. (2016) 1–6.
[36] G.R. Warrier, V.K. Dhir, Heat transfer and wall heat flux partitioning during subcooled flow nucleate boiling: a review, J. Heat Transfer 128 (12) (2006) 1243–1256.
[37] N. Kurul, M.Z. Podowski, Multidimensional effects in forced convection subcooled boiling, Proceedings of the Ninth International Heat Transfer Conference, vol. 2, Hemisphere Publishing, New York, 1990, pp. 19–24.

[38] L. Gilman, E. Baglietto, A self-consistent, physics-based boiling heat transfer modeling framework for use in computational fluid dynamics, Int. J. Multiph. Flow 95 (2017) 35–53.
[39] J. Buongiorno, D. Cahill, C. Hidrovo, S. Moghaddam, A. Schmidt, L. Shi, Micro-and nanoscale measurement methods for phase change heat transfer on planar and structured surfaces, Nanosc. Microsc. Thermophys. Eng. 18 (3) (2014) 270–287.
[40] C. Gerardi, Investigation of the Pool Boiling Heat Transfer Enhancement of Nano-Engineered Fluids by Means of High-Speed Infrared Thermography, Ph. D. thesis, Massachusetts Institute of Technology, 2009.
[41] V. Dhir, Simulation of boiling: How far have we come!, in: Proceedings of 7th ECI International Conference on Boiling Heat Transfer, Florianópolis, Brazil, May, 2009, pp. 3–7.
[42] S. Van Stralen, M. Sohal, R. Cole, W. Sluyter, Bubble growth rates in pure and binary systems: combined effect of relaxation and evaporation microlayers, Int. J. Heat Mass Transf. 18 (3) (1975) 453–467.
[43] S. Popinet, An accurate adaptive solver for surface-tension-driven interfacial flows, J. Comput. Phys. 228 (16) (2009) 5838–5866.
[44] A. Rednikov, P. Colinet, Singularity-free description of moving contact lines for volatile liquids, Phys. Rev. E 87 (1) (2013) 010401.
[45] J. Moriarty, L. Schwartz, Effective slip in numerical calculations of moving-contact-line problems, J. Eng. Math. 26 (1) (1992) 81–86.
[46] O. Weinstein, L. Pismen, Scale dependence of contact line computations, Math. Model. Nat. Phenom. 3 (1) (2008) 98–107.
[47] S. Afkhami, S. Zaleski, M. Bussmann, A mesh-dependent model for applying dynamic contact angles to VOF simulations, J. Comput. Phys. 228 (15) (2009) 5370–5389.
[48] S. Afkhami, J. Buongiorno, A. Guion, S. Popinet, R. Scardovelli, S. Zaleski, Transition in a Numerical Model of Contact Line Dynamics and Forced Dewetting, arXiv preprint arXiv:1703.07038.
[49] M. Cooper, A. Lloyd, The microlayer in nucleate pool boiling, Int. J. Heat Mass Transf. 12 (8) (1969) 895–913.
[50] B. Mikic, W. Rohsenow, P. Griffith, On bubble growth rates, Int. J. Heat Mass Transf. 13 (4) (1970) 657–666.
[51] C.R. Kharangate, I. Mudawar, Review of computational studies on boiling and condensation, Int. J. Heat Mass Transf. 108 (2017) 1164–1196.
[52] R. Scardovelli, S. Zaleski, Direct numerical simulation of free-surface and interfacial flow, Ann. Rev. Fluid Mech. 31 (1) (1999) 567–603.
[53] S. Popinet, Gerris: a tree-based adaptive solver for the incompressible euler equations in complex geometries, J. Comput. Phys. 190 (2) (2003) 572–600.
[54] S. Popinet, Numerical models of surface tension, Ann. Rev. Fluid Mech. 50 (2018) 49–75.
[55] S. Afkhami, M. Bussmann, Height functions for applying contact angles to 2D VOF simulations, Int. J. Numer. Meth. Fluids 57 (4) (2008) 453–472.
[56] G. Taylor, D. Michael, On making holes in a sheet of fluid, J. Fluid Mech. 58 (04) (1973) 625–639.
[57] M.P. Brenner, D. Gueyffier, On the bursting of viscous films, Phys. Fluids 11 (3) (1999) 737–739.
[58] N. Savva, J.W. Bush, Viscous sheet retraction, J. Fluid Mech. 626 (2009) 211–240.
[59] L. Gordillo, G. Agbaglah, L. Duchemin, C. Josserand, Asymptotic behavior of a retracting two-dimensional fluid sheet, Phys. Fluids 23 (12) (2011) 122101.
[60] G. Agbaglah, C. Josserand, S. Zaleski, Longitudinal instability of a liquid rim, Phys. Fluids 25 (2) (2013) 022103.
[61] A. Guion, Modeling and Simulation of Liquid Microlayer Formation and Evaporation in Nucleate Boiling Using Computational Fluid Dynamics, Ph.D. thesis, Massachusetts Institute of Technology, 2017.